

# A Hybrid Protein–Polymer Nanoworm Potentiates Apoptosis Better than a Monoclonal Antibody

Suhaas Rayudu Aluri,<sup>†</sup> Pu Shi,<sup>†</sup> Joshua A. Gustafson,<sup>†</sup> Wan Wang,<sup>†</sup> Yi-An Lin,<sup>‡</sup> Honggang Cui,<sup>‡</sup> Shuanglong Liu,<sup>§</sup> Peter S. Conti,<sup>§,†,||</sup> Zibo Li,<sup>§</sup> Peisheng Hu,<sup>†</sup> Alan L. Epstein,<sup>†</sup> and John Andrew MacKay<sup>†,||,\*</sup>

<sup>†</sup>Department of Pharmacology and Pharmaceutical Sciences, University of Southern California, Los Angeles, California 90033, United States, <sup>‡</sup>Department of Chemical and Biomolecular Engineering, Johns Hopkins University, Baltimore, Maryland 21218, United States, <sup>§</sup>Department of Radiology, Keck School of Medicine, University of Southern California, Los Angeles, California 90089, United States, <sup>||</sup>Department of Pathology, Keck School of Medicine, University of Southern California, Los Angeles, California 90089, United States, and <sup>||</sup>Department of Biomedical Engineering, University of Southern California, Los Angeles, California 90089, United States,

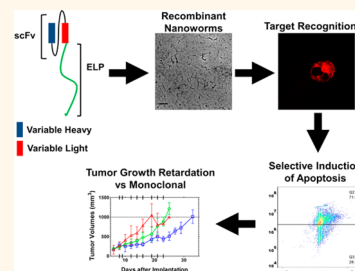
**ABSTRACT** B-cell lymphomas continue to occur with a high incidence. The chimeric antibody known as Rituximab (Rituxan) has become a vital therapy for these patients. Rituximab induces cell death via binding and clustering of the CD20 receptor by Fc $\gamma$  expressing effector cells. Because of the limited mobility of effector cells, it may be advantageous to cluster CD20 directly using multivalent nanostructures. To explore this strategy, this manuscript introduces a nanoparticle that assembles from a fusion between a single chain antibody and a soluble protein polymer. These hybrid proteins express in *Escherichia coli* and do not require bioconjugation between the antibody and a substrate. Surprisingly a fusion between an anti-CD20 single chain antibody and a soluble protein polymer assemble worm-like nanostructures, which were characterized using light scattering and cryogenic transmission electron microscopy. These nanoworms competitively bind CD20 on two B-cell lymphoma cell lines, exhibit concentration-dependent induction of apoptosis, and induce apoptosis better than Rituximab alone. Similar activity was observed *in vivo* using a non-Hodgkin lymphoma xenograft model. In comparison to Rituximab, systemic nanoworms significantly slowed tumor growth. These findings suggest that hybrid nanoworms targeted at CD20 may be useful treatments for B-cell related malignancies. Because of the ubiquity of antibody therapeutics, related nanoworms may have uses against other molecular targets.

**KEYWORDS:** elastin like polypeptides · b-cell lymphomas · Rituxan · Rituximab anti-CD20 · hyper-cross-linking · lipid rafts · apoptosis · tumor xenograft · biodistribution · nanoworms

**A**ntibody fragments have potential advantages over intact antibodies.<sup>1,2</sup> Single chain variable regions (scFv) are antibody fragments that have pharmaceutical potential<sup>3</sup> because they are simple to express and modify,<sup>4</sup> can carry drugs or imaging agents,<sup>4,5</sup> have small size compared to antibodies,<sup>4,6–8</sup> and have relatively short half-lives ( $\sim$ 4 h).<sup>7</sup> The short half-life can yield a high signal-to-noise ratio in imaging applications but may be detrimental to their use as therapeutics.<sup>9,10</sup> The half-lives of recombinant scFv fragments can be prolonged by bioconjugation to high molecular weight hydrophilic polymers.<sup>11,12</sup> In this manuscript, we describe novel recombinant scFv nanoparticles that target cell-surface receptors, initiate apoptosis, and may be useful to manage B-cell lymphomas. What is innovative about the approach

herein is that the scFv expressed as a fusion with a protein polymer, which eliminates the need for chemical bioconjugation. To a surprising degree, these hybrid protein polymer nanoparticles have potent therapeutic effects.

Lymphomas have an incidence rate of 27 in 100 000 people per year.<sup>13</sup> Non-Hodgkin lymphomas, mostly of B-cell origin (~85%), are the most prevalent with around 79 000 patients expected to be diagnosed in 2013.<sup>13</sup> Therapies includes the use of a combination chemotherapy regimen (e.g., CHOP, ABCVP), which often includes the antibody Rituximab.<sup>14–16</sup> Rituximab is a chimeric antibody that binds the B-cell surface marker, CD20, which is expressed in pre- to mature B-cells. Rituximab also has clinical activity as a single agent in multiple indolent lymphomas.<sup>17</sup> As a single agent,



\* Address correspondence to jamackay@usc.edu.

Received for review July 30, 2013 and accepted January 31, 2014.

Published online January 31, 2014  
10.1021/nn403973g

© 2014 American Chemical Society

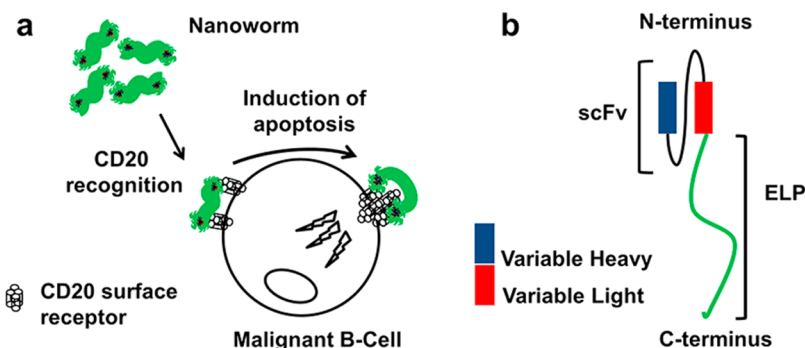


**Figure 1.** Hybrid protein polymer nanoworms designed to enhance apoptotic signaling. (a) Expression of a fusion between a single chain antibody (scFv) and a protein polymer yields stable nanoworms. The nanoworms target cell-surface CD20 receptor, inducing apoptosis in B-cells, and hence may have application for lymphoma therapies. (b) An anti-CD20 scFv consisting of both a heavy and light chain was fused to the amino terminus of an elastin-like polypeptide (ELP). The ELP protein polymer, A192, was selected to promote solubility at physiological conditions and receptor clustering upon binding the cell surface.

**TABLE 1. Biophysical Characteristics of Purified ELP Fusions**

ELP	amino acid sequence <sup>a</sup>	T <sub>t</sub> (°C) <sup>b</sup>	behavior	apparent/expected MW (kDa) <sup>c</sup>
A192	G(VPGAG) <sub>192</sub> Y	55.1	unimeric	73.4/73.6
scFv-A192	QVQLQPGAEKLVKPGASVKSCKASGYTFTSYNMHWVKQTGRLWIGAIYPGNGDTSYNQKFKG-KATLTADKSSSTAYMQLSSLTEADAVYYCARSTYYGGDWYFNVWGAGTVTVSAGGGSGGGSG-GGGSQVLSQSPLAISASPGEKVMTCRASSSVYIHWFQQKPGSSPKWIYATSNLASGVPVRS-GSGSGTYSLTLRVEADAATYYCQQWTSNPPTFGGGTKLEIKRTG(VPGAG) <sub>192</sub> Y	42.0	nanoworm	99.6/99.1

<sup>a</sup> Gene sequences confirmed by DNA sequencing from N and C termini. <sup>b</sup> Transition temperature (25 μM, pH 7.4) determined by optical density measurements at 350 nm.

<sup>c</sup> Molecular weight estimated using SDS-PAGE. Expected molecular weight based on amino acid sequence.

Rituximab is thought to function through (i) direct induction of cell apoptosis, (ii) complement activation, and (iii) antibody-dependent cell cytotoxicity.<sup>18</sup> Interestingly, Rituximab induction of apoptosis is enhanced when cross-linked *via* anti-Fc antibodies<sup>19,20</sup> or Fcγ receptors.<sup>21</sup> Cross-linking CD20 promotes translocation of the CD20 complex into lipid rafts, causing inhibition of P38 MAPK and ERK1/2 survival pathways.<sup>22–24</sup> This apoptotic mechanism has been utilized by various groups to design therapeutic systems utilizing multivalent Fab<sup>25</sup> and Fab polymer conjugates.<sup>19,26</sup> These constructs have potent *in vitro* and *in vivo* activity, which suggests that antibody cross-linking is a viable strategy. This strategy makes CD20 a rational proof-of-concept for evaluating scFv-based fusion proteins.

To exploit CD20 dependent apoptosis, an anti-CD20 recombinant scFv was fused (Figure 1a, Table 1) with an elastin-like polypeptide (ELP). The ELP is a hydrophilic protein polymer with pentameric repeats of [Val-Pro-Gly-Xaa-Gly]<sub>n</sub>, where Xaa can be any amino acid. These polypeptides undergo a reversible phase separation above a tunable transition temperature, which depends on Xaa and n.<sup>27</sup> The recombinant fusion was designed with a Rituximab-derived scFv fragment fused to the N-terminus of a 73.6 kDa molecular weight ELP (Figure 1b). This protein polymer tag enables quick and efficient purification *via* temperature cycling, serves as a biodegradable carrier, and may reduce the renal clearance of scFvs. Genetic engineering

and biological synthesis allow for accurate control over length and sequence, and by designing the construct as a direct hybrid of the scFv and protein polymer, subsequent chemical bioconjugation is unnecessary. Additionally, the lower cost of bacterial expression may be commercially attractive in comparison with mammalian-cell expression of monoclonal antibodies.

## RESULTS

**scFv Fusions Form Nanoparticles at Physiological Temperatures.** The fusion protein called scFv-A192 was purified from bacterial lysate by triggering the phase separation of the ELP A192 (Table 1). The yield of the fusion ranged from 20 to 30 mg/L of bacterial culture. The purity determined through Coomassie SDS-PAGE was 91.4 ± 1.3% (Figure 2a). The purified fusion retained its phase separation properties (Figure S1a, Supporting Information) but transitioned at a lower temperature when fused to the scFv (Figure S1b, Supporting Information). The scFv-A192 fusion phase separates above ~42 °C, while A192 alone phase separates above ~55 °C. At physiological temperature, dynamic light scattering revealed that scFv-A192 formed nanoparticles with a hydrodynamic radius of 85.7 ± 16.5 nm (Figure 2b). The radius for unmodified A192 is 6.7 ± 0.2 nm, which suggests that the scFv domain mediates nanoparticle assembly (Figure 2b). Below its transition temperature, A192 alone does not mediate particle

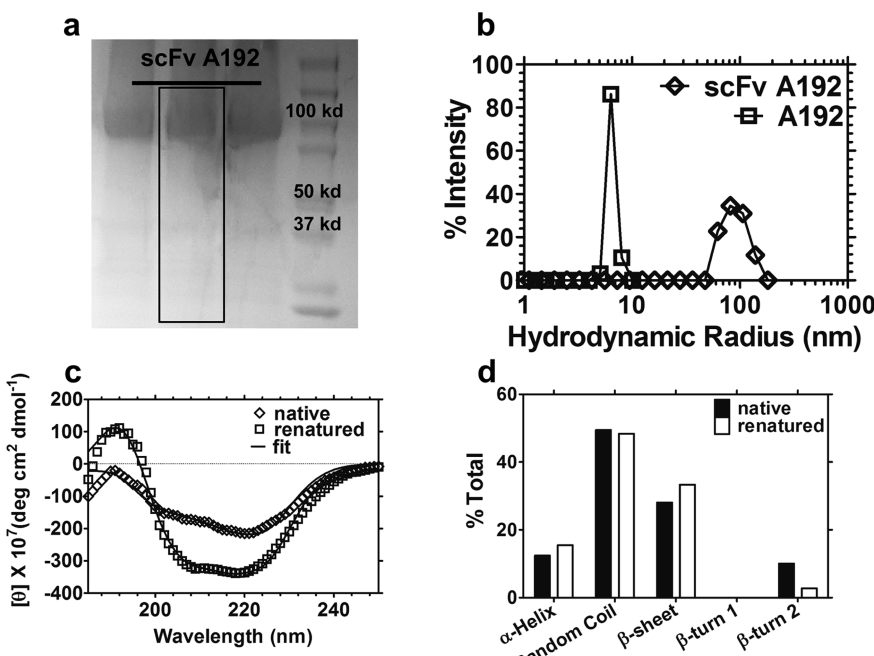


**Figure 2.** Purified scFv-A192 forms nanoparticles whose secondary structure is stabilized by renaturation. (a) Purified scFv-A192 on a 4–20% SDS-PAGE shows a MW of ~99.6 kDa and a purity of  $91.4 \pm 1.3\%$ . Outlined lanes were used to determine protein purity using ImageJ. (b) scFv-A192 assembles nanoparticles with a hydrodynamic radius of  $85.7 \pm 16.5$  nm. (c) Changes in protein structure during refolding were characterized by circular dichroism, which show a significant shift in spectra at 190 and 220 nm. (d) Deconvolution of the curves showed a substantial decrease in  $\beta$ -turn 2 content. The lowering of the  $\beta$ -turn content suggests a change in the ELP secondary structure.

assembly; therefore, a likely interpretation is that the scFv forms the core of a nanoparticle.

**Renaturation of the scFv Fusion Stabilizes Secondary Structure and Forms Nanoworms.** To address the unexpected assembly of scFv-A192 into nanoparticles, they were disrupted using chaotropic salt (6 M Guanidine) and renatured under dialysis. The secondary structure and particle dimensions were compared before disruption (native) and after renaturation. Using circular dichroism, the secondary structure of native scFv-A192 particles showed no single characteristic spectra (Figure 2c); however, deconvolution revealed a mixture of secondary structures including type 2  $\beta$ -turns that are often observed on ELPs (Figure 2d). Renaturation caused a substantial change in secondary structure, which was associated by a reduction in  $\beta$ -turn content (Figure 2d). By replacing these turns with  $\beta$ -sheets, renaturation may increase the persistence length of the ELPs stabilizing the corona of these nanostructures. Similar to the native nanoparticles, the renatured sample was stable up to 41 °C (Figure S2, Supporting Information). No phase separation was observed under normothermic conditions (~37 °C), which suggested that these nanostructures are suitable for therapeutic exploration.

Microscopy of native scFv-A192, utilizing cryogenic transmission electron microscopy (cryoTEM), confirmed monodisperse spherical particles in solution with a diameter of  $48.1 \pm 11.8$  nm (Figure 3a,c). In contrast, the renatured nanoparticles showed a major

population of high aspect ratio nanoparticles with lengths of  $56.2 \pm 15.9$  nm and widths of  $17.9 \pm 3.5$  nm (Figure 3b,d). A minor population of spherical particles with a diameter of  $27.4 \pm 7.5$  nm was also observed (Figure 3b). The round particles may also be nanoworms with their long axes parallel to the electron beam. On the basis of their size, composition, and morphology, these renatured nanoparticles are defined as hybrid protein polymer nanoworms.

The nanostructures were compared independently using multiangle light scattering. Analysis performed on native scFv-A192 confirmed assembly of particles with an absolute molecular weight of 25 490 kDa (Figure 3e). In addition to confirming assembly of particles with a radius of gyration ( $R_g$ ) of  $47.7 \pm 0.1$  nm, the absolute molecular weight suggests that particles are made up of an average of ~250 scFv-A192 monomers (Figure 3e). In fact, the refolded particles showed a significant reduction in absolute molecular weight giving rise to a mixture of 8372 and 8073 kDa particles (Figure 3f). The reduction in absolute molecular weight translates to about 80 scFv-A192 monomers making up the nanoworms. The two populations have similar absolute molecular weight but with varying radii of gyration of  $45.2 \pm 0.1$  and  $33.7 \pm 0.1$  nm, respectively (Figure 3f). Because of limitations of dynamic light scattering, only a single population with a hydrodynamic radius ( $R_h$ ) of  $65.3 \pm 15.5$  nm could be identified. The  $R_g/R_h$  ratios were used to interpret the morphology changes due to refolding. The native scFv-A192 had an

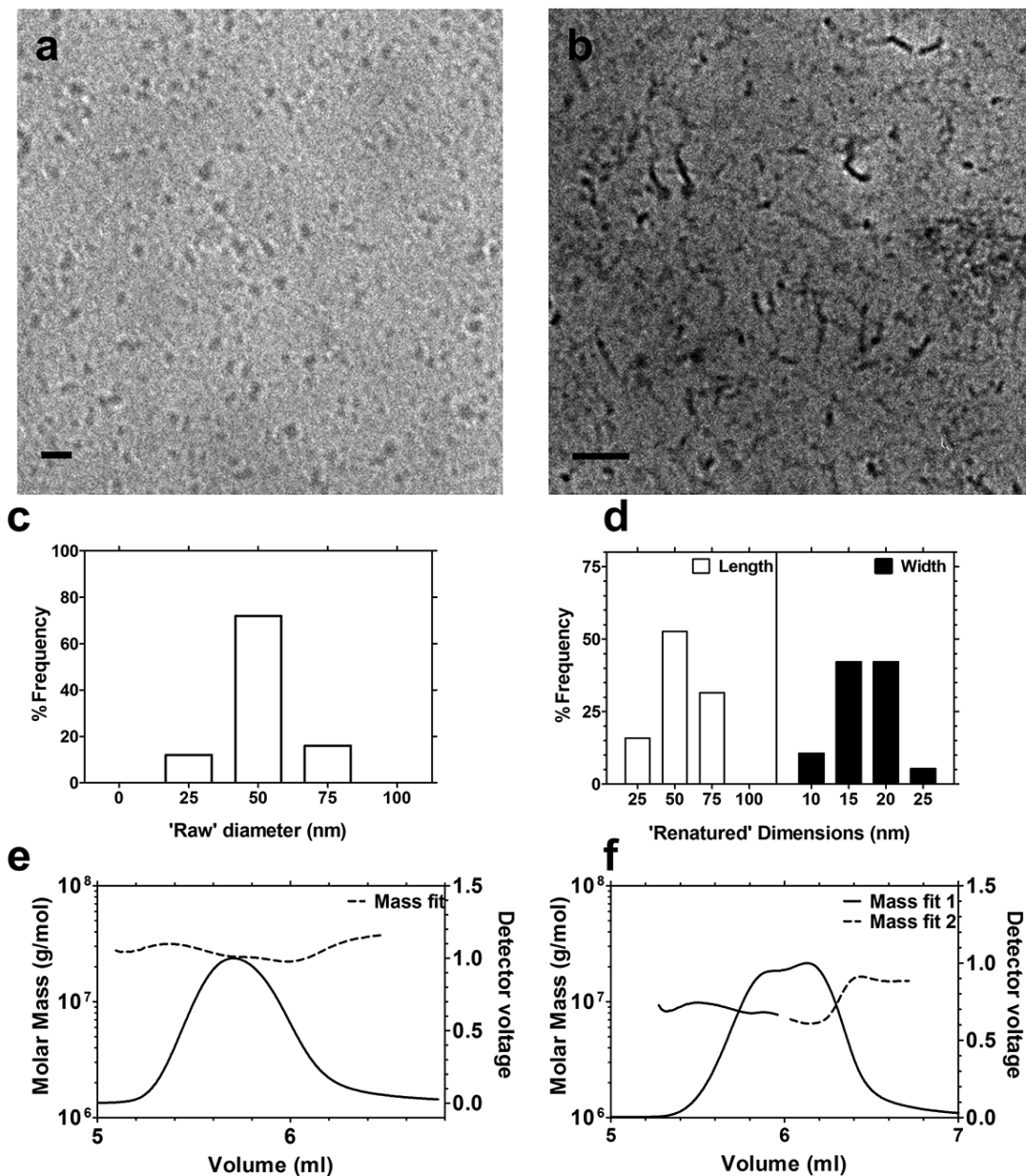


**Figure 3.** Renaturation of scFv-A192 is required to form high-aspect ratio nanoworms. (a) cryoTEM images of native scFv-A192 shows assembly of spherical assemblies with a diameter of  $48.1 \pm 11.8$  nm. (b) scFv-A192 was denatured with guanidine hydrochloride and renatured using dialysis. cryoTEM images of renatured particles show a dominant species of high aspect ratio nanoworms with lengths of  $56.2 \pm 15.9$  nm and a minor population of spherical structures with a diameter of  $27.4 \pm 7.5$  nm. (c) The distribution of particle diameters of native scFv-A192 particles. (d) The distribution of particle dimensions of renatured nanoworms. (e) Multiangle light scattering analysis on native particles show a molecular weight of 25 490 kDa and a radius of gyration ( $R_g$ ) of  $47.7 \pm 0.1$  nm. (f) In contrast, analysis of the renatured nanoworms showed a population of 8372 kDa (mass fit 1) and 8073 kDa (mass fit 2) with  $R_g$  of  $45.2 \pm 0.1$  and  $33.7 \pm 0.1$  nm, respectively. Scale bars represent 100 nm.

$R_g/R_h$  of 0.56. The low  $R_g/R_h$  value for the scFv-A192 (<0.7 for polymeric micelles) is consistent with the assembly of spherical particles with a densely packed core.<sup>28,29</sup> In contrast, the renatured scFv-A192 consists of two populations with slightly different shapes and packing densities. One of these populations had an estimated  $R_g/R_h$  of 0.7 after renaturation, which is consistent with the formation of high aspect ratio nanoparticles. Thus, data obtained through light scattering experiments is consistent

with the cryoTEM observations of these hybrid nanoworms.

**Nanoworms Target the CD20 Surface Receptor *In Vitro*.** Rhodamine-labeled Rituximab and recombinant nanoworms successfully recognized two CD20+ B-cell lymphomas (Figure 4). Rituximab efficiently bound CD20 with equal distribution on the cell surface (Figure 4a(i–iii, vii–xi)). On addition of a secondary goat antihuman Fc antibody (GAH), the surface-bound Rituximab showed a speckled or punctate pattern

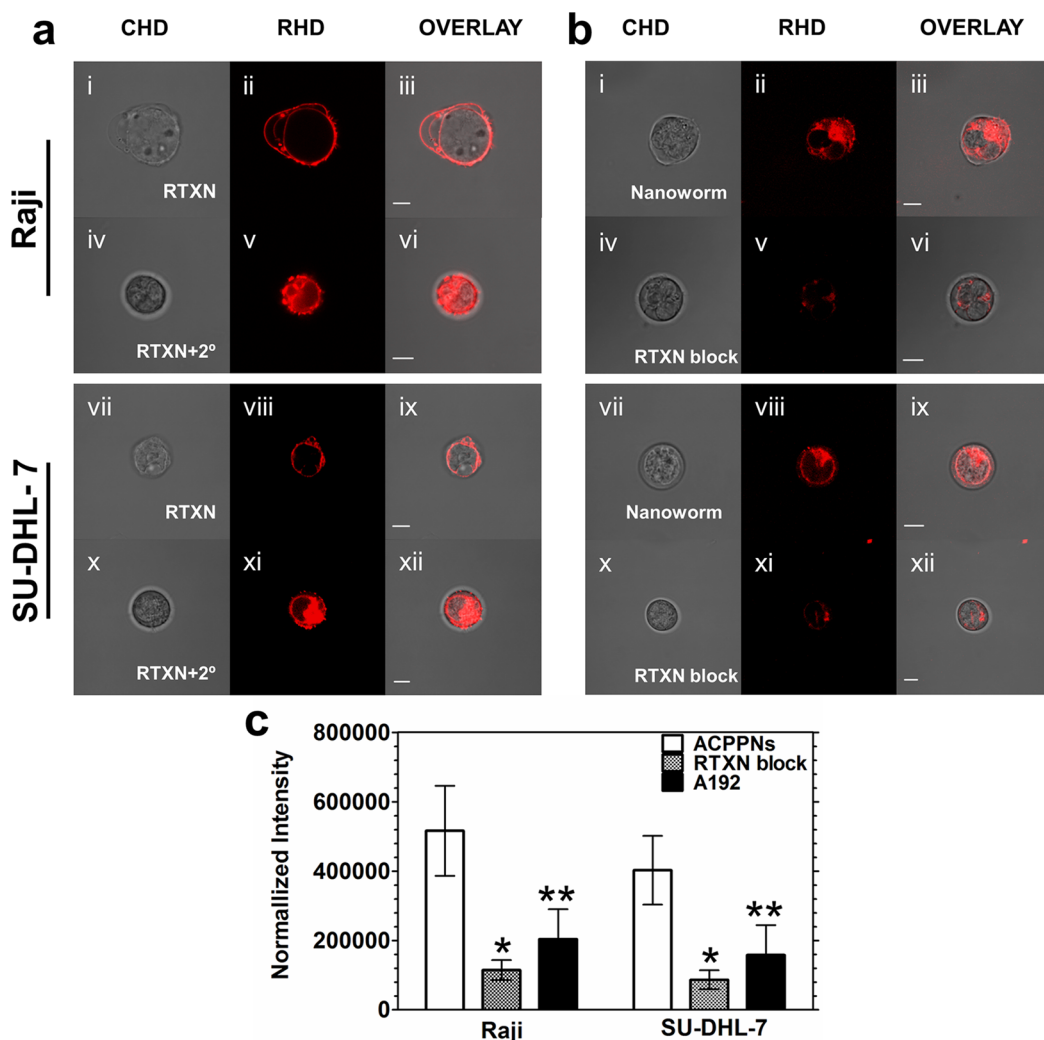


**Figure 4.** Recombinant nanoworms competitively target CD20<sup>+</sup> cells. Confocal laser scanning microscopy was used to compare the uptake of rhodamine-labeled monoclonal Rituximab and nanoworms on two CD20<sup>+</sup> cell lines, Raji and SU-DHL-7. (a) Panels i–iii and vii–ix show CD20 recognition by labeled Rituximab on Raji and SU-DHL-7 cells, respectively. Rituximab forms a surface-bound ring pattern around the target cell. Panels iv–vi and x–xii show that coincubation of labeled Rituximab with a secondary GAH antibody (2°) causes Rituximab sequestration on cell surface. (b) Panels i–iii and vii–xi show recognition of surface CD20 by labeled nanoworms. The nanoparticles bind and cause receptor sequestration similar to cross-linked Rituximab. Panels iv–vi and x–xii show that preincubation with unlabeled Rituximab blocks binding of labeled nanoworms. (c) A quantitative analysis of the normalized fluorescent intensity was calculated using ImageJ ( $n = 4$  slides). This revealed that nanoworm binding was significantly higher than for labeled A192 or nanoworm blocked by Rituximab (unpaired 2 tailed  $t$  test,  $\alpha = 0.05$ ,  $P = 0.026^*$ ,  $0.04^{**}$ ). Scale bar represents  $5 \mu\text{m}$ .

within the cell due to translocation of cross-linked Rituximab into lipid rafts (Figure 4a(iv–vi, x–xii)). In both CD20<sup>+</sup> cell lines, the rhodamine-labeled nanoworms bound in a pattern similar to cross-linked Rituximab (Figure 4b(i–iii, vii–ix)). To demonstrate that the nanoworms bind to the same molecular target as Rituximab, binding was blocked with unlabeled Rituximab (Figure 4b(iv–vi, x–xii)). When quantified through image analysis, the data demonstrates that the nanoworm binding to both CD20<sup>+</sup> cell lines can be blocked by pretreatment with unlabeled Rituximab (Figure 4c). Similarly, a rhodamine-labeled A192 polymer has low binding to both cell lines (Figures 4c and S4a, Supporting Information). In contrast, both Rituximab and nanoworms showed

minimal binding to CD20<sup>-</sup> CEM cells (Figure S3a,b, Supporting Information).

#### Nanoworms Reduce B-Cell Viability by Inducing Apoptosis.

Preliminary experiments with trypan blue exclusion showed a significant increase in trypan positive cells when CD20<sup>+</sup> B-cells were treated with increasing concentrations of nanoworms (Figure 5a). A formazan (MTS/PMS) based colorimetric assay confirmed a concentration-dependent reduction in cell viability with an inhibitory concentration ( $\text{IC}_{50}$ ) of 32, 41  $\mu\text{M}$  in Raji, SU-DHL-7 cells, respectively (Figure 5b). When treated with nanoworms, the CD20<sup>-</sup> CEM cells showed only minimal reductions in viability (Figure 5b). Similarly, Rituximab treatment alone showed minimal effect on the viability of Raji cells, which prevented the

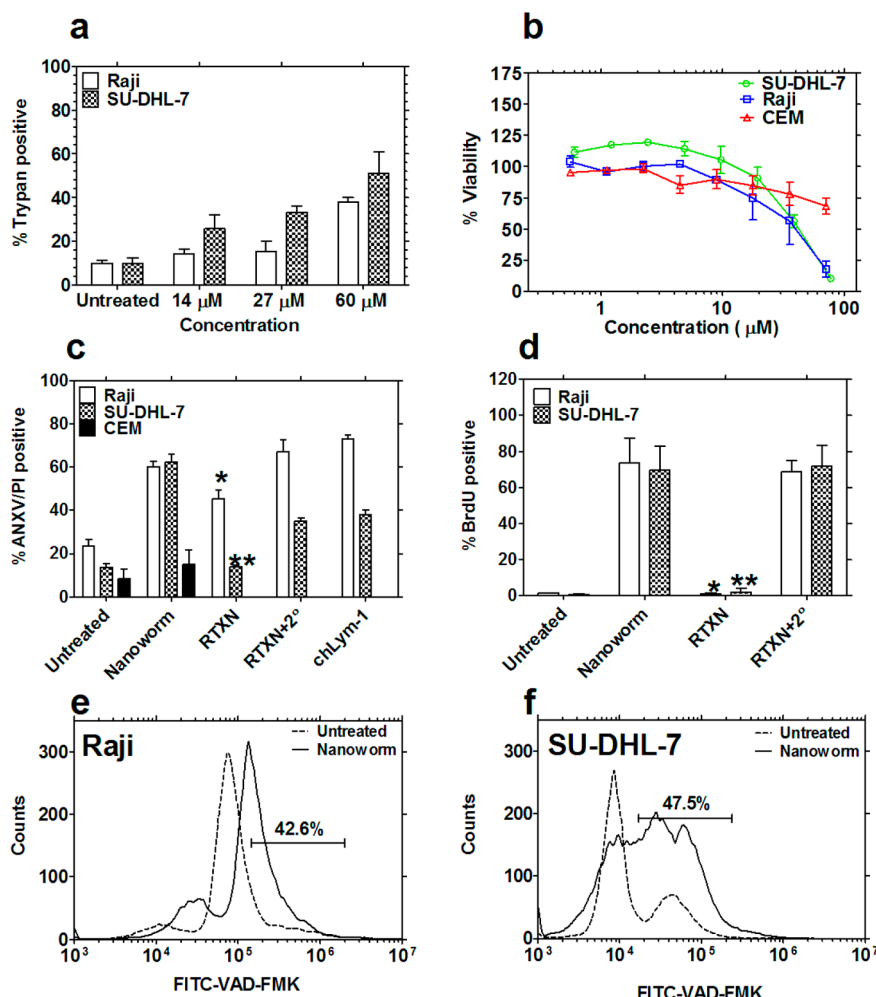


**Figure 5. Nanoworms reduce viability of CD20+ human lymphoma cell lines by inducing apoptosis.** (a) Trypan blue exclusion showed a significant increase in trypan blue positive cells with increasing concentrations of nanoworms. (b) CD20+ cells, Raji and SU-DHL-7, show a concentration-dependent reduction in cell viability. The calculated IC<sub>50</sub>s for Raji and SU-DHL-7 are 32 and 41 μM, respectively; CD20− CEM are less affected by nanoworm treatment. The extrapolated IC<sub>50</sub> for CEM cells is 294 μM, which is 10 times higher than tested CD20+ cell lines. (c) Raji and SU-DHL-7 cells both show a significant increase in annexin V/Propidium iodide staining after nanoworm treatment when compared to plain Rituximab ( $P = 0.003^*$ ,  $P = 0.0005^{**}$ ). Rituximab cross-linked by secondary GAH and apoptosis control, chLym-1, both induce apoptosis. (d) TUNEL staining confirms nanoworm induction of apoptosis. The nanoparticles outperform Rituximab in both cell lines ( $P = 0.006^*$ ,  $P = 0.006^{**}$ ). Nanoworms induce apoptosis to the same extent as secondary GAH cross-linked Rituximab. (e,f) Nanoworm treatment substantially increased caspase activity in both Raji and SU-DHL-7 cells.

determination of an IC<sub>50</sub> (Figure S3c, Supporting Information). Rituximab did show concentration-dependent reduction in viability for SU-DHL-7 cells, which resulted in an IC<sub>50</sub> of 4.8 μM (Figure S3c, Supporting Information).

Induction of early and late stage apoptosis was detected by annexin V/propidium iodide and TUNEL staining, respectively. All fusion proteins were compared with an equivalent Fv dose of 1.5 mg/mL. Nanoworms significantly enhanced induction of early apoptosis in both CD20+ cell lines as detected using annexin V/propidium iodide staining when compared to Rituximab alone (unpaired 2 tail *t* test,  $\alpha = 0.05$ ,  $P = 0.003^*$ ,  $P = 0.0005^{**}$ ). Rituximab dosed at the same single chain concentration showed variable induction of apoptosis in CD20+ cell lines with Raji cells

responding better than SU-DHL-7 cells (Figure 5c). On cross-linking Rituximab with a secondary GAH, both cell lines showed an increase in early apoptosis. Since nanoworms induce apoptosis on binding, a positive control antibody, Chimeric Lym-1 (chLym-1), with a similar mechanism of action was used. The chLym-1 control is an anti-HLA-Dr10 antibody, which is an effective inducer of apoptosis on direct cell binding (Figure 5c).<sup>30,31</sup> Treatment with an equivalent single chain dose of chLym-1 performed slightly better than the recombinant nanoparticle in Raji cells but was less effective in SU-DHL-7 cells. The variable response could be due to a lower expression of surface HLA-Dr10 on SU-DHL-7 cells (Figure 5c).<sup>32</sup> Unlike chLym-1, the nanoworm was equally potent in both cell lines. CEM cells treated with the nanoworm showed minimal induction

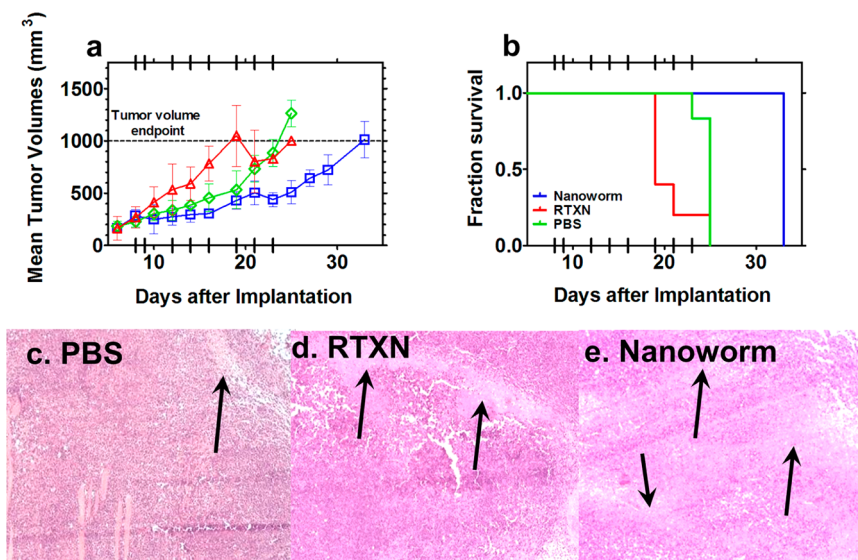


**Figure 6. Nanoworm treatment significantly reduces tumor burden in Raji xenografts.** (a) Tumor regression studies were repeated with renatured nanoworms (2.5 mg/dose), Rituximab (1.7 mg/dose) and PBS. As of day 25, nanoworms significantly reduced mean tumor burden when compared to PBS and Rituximab treated groups ( $n = 5/\text{group}$ ,  $\alpha = 0.05$ ,  $P = 0.0011$ ). (b) Nanoworm treatment significantly enhances survival when compared to PBS and Rituximab control groups ( $\alpha = 0.05$ ,  $P = 0.013$ ). The highlighted tick marks indicate days of dose administration. (c–e) Tumors from Rituximab and nanoworm treated groups show larger necrotic areas (arrows) when compared to PBS group. Three sections per mouse ( $n = 3$ ) were analyzed from nanoworms, Rituximab, and PBS treated groups. The number of slides with observable necrotic areas in nanoworms, Rituximab, and PBS are 8, 7, and 3 slides (of 9 total slides in each group), respectively. Images of slices were taken using a 5 $\times$  objective.

of apoptosis and hence were not evaluated further (Figure 5c). Unmodified A192 showed minimal binding of CD20+ cells and induced minimal levels of apoptosis at an equivalent concentration (Figure S4a,b, Supporting Information).

TUNEL staining was used to determine the induction of late apoptosis because annexin V/propidium iodide staining is known to detect early apoptosis. All proteins were compared with an equivalent Fv dose of 2.5 mg/mL. The nanoworms significantly enhance apoptosis compared to plain Rituximab (unpaired 2 tail  $t$  test,  $\alpha = 0.05$ ,  $P = 0.006^*$ ,  $P = 0.006^{**}$ ) in both CD20+ cell lines (Figure 5d). The efficacy of Rituximab can be enhanced to the same extent as the particle by cross-linking with secondary GAH (Figure 5d). Subsequently, the activation of apoptotic caspase cascade was confirmed using FITC-VAD-FMK (Figure 5e,f). A substantial increase in the FITC signal was observed after treatment with nanoworms, in both Raji and SU-DHL-7 cells. The activation of the caspase cascade by the nanoworm is similar to hypercrosslinked Rituximab<sup>19</sup> and may activate the same molecular pathway. Hence the nanoworms are effective inducers of apoptosis in both B-cell lymphoma cell lines and outperform Rituximab *in vitro*.

**Nanoworm Tumor Regression and Biodistribution Studies.** Having demonstrated that the nanoworms are specific for CD20 and efficiently mediate cellular apoptosis, their potential therapeutic applications were probed in Raji xenografted athymic nude mice. Tumor regression studies were performed with Raji xenografts implanted

in the right flank of athymic nude mice ( $n = 5/\text{group}$ ). The mice were administered a total of 8 doses, and tumor volume was monitored until the tumor volume end point (1000 mm<sup>3</sup>) was reached. Nanoworm treatment significantly slowed tumor growth compared to Rituximab and phosphate buffered saline (PBS) groups (Figure 6a). Repeated measures 1-way ANOVA performed on the mean tumor volumes show a significant difference between all three treatment groups ( $\alpha = 0.05$ ,  $P = 0.0011$ ). Post hoc analysis revealed a statistically significant difference between the nanoworms, Rituximab (Tukey HSD,  $P = 0.0015$ ), and PBS (Tukey HSD,  $P = 0.018$ ) treatment. Tumor volumes of Rituximab and PBS showed no statistically significant difference (Tukey HSD,  $P = 0.148$ ). Nanoworms significantly improved survival when compared to Rituximab and PBS treatment groups (Log rank test,  $\alpha = 0.05$ ,  $P = 0.013$ , Figure 6b). The median survival times for nanoworms, Rituximab, and PBS were 33, 19, and 25 days, respectively. Individual tumor growth curves are plotted in Figure S5, Supporting Information. The administered doses were adequately tolerated but produced a weight loss (~20%) observed in the test group after the first two doses (Figure S6, Supporting Information). The weight was recovered by day 13 in all subjects. The dry weight of the organs harvested from three groups ( $n = 3$ ) did not change appreciably; however, a slight increase in dry spleen weight was observed in Rituximab and nanoworm groups when compared to the PBS treatment group (Table S1, Supporting Information). Similarly, major organs collected showed

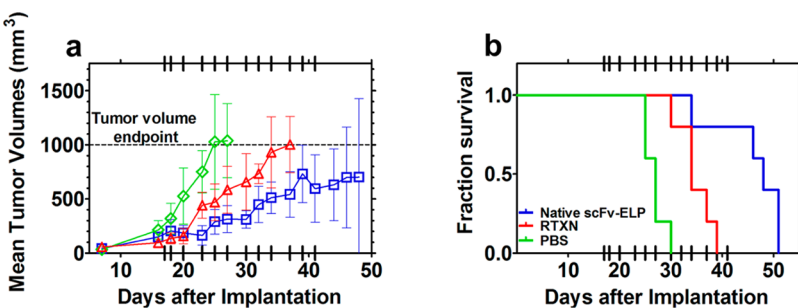


**Figure 7.** Native scFv-A192 treatment improves survival in Raji xenografted nude mice. (a) Raji tumors grafted onto nude mice were treated with native scFv-A192 (2.5 mg/dose), Rituximab (30  $\mu$ g/dose), and PBS. Mean tumor volumes showed a slightly significant difference between native scFv-A192, Rituximab, and PBS treated groups ( $n = 5$ /group,  $\alpha = 0.05$ ,  $P = 0.047$ ) on day 27. Post hoc analysis revealed no statistically significant difference between native scFv-A192, and Rituximab. (b) Native scFv-A192 treatment significantly improved survival when compared to Rituximab and PBS treatment groups ( $\alpha = 0.05$ ,  $P = 0.002$ ). The median survival times for native scFv-A192, Rituximab, and PBS were 48, 34, and 27 days, respectively.

no observable histological changes in the three groups except for the tumor (Figure 6c–e). The tumors in the Rituximab and nanoworm treatment groups showed similar histology with prominent necrotic regions compared to that seen in the PBS groups. While the focus of this manuscript is the efficacy of the renatured nanoworm, the native scFv-A192 also had partial efficacy.

In an independent study, native scFv-A192 did show inhibition of tumor growth; however, a significant difference in efficacy was not detected when compared to a low dose of Rituximab (Figure 7). The poor response to Rituximab has been observed previously in this model<sup>33,34</sup> and could be due to a variety of factors. Rituximab accumulation in tumor is inversely proportional to tumor burden; i.e. small tumor volumes have high Rituximab tumor accumulation.<sup>35</sup> The lack of Fc:FcR interactions in a subcutaneous murine model leads to poor activation of human Fc-mediated antibody dependent cellular cytotoxicity and complement dependent cytotoxicity-mediated tumor regression and could lead to poor efficacy of chimeric Rituximab.<sup>34</sup> Because of poor CD20 cross-linking by Rituximab *in vivo*, the efficacy of treatment could be drastically reduced. In contrast, the nanoworms are inherently multivalent and do not require subsequent cross-linking to potentiate CD20-mediated apoptosis.

A microbiodistribution study of rhodamine-labeled nanoworms ( $n = 3$ ) showed accumulation in various organs (Figure 8a–h). The labeled nanoworm signal was seen in the liver (Figure 8a,e), spleen (Figure 8b,f), tumor (Figure 8c,g), and kidney (Figure 8d,h). Minimal accumulation was observed in the heart and lungs. A biodistribution study performed on Raji xenografted mice using <sup>64</sup>Cu assisted positron emission tomography study ( $n = 3$ ) confirms the high splenic and hepatic accumulation of the particles. The half-life of the heart signal, which predominantly reflects the blood half-life, was estimated at  $109.5 \pm 31.4$  min (Figure 8i,j).

## DISCUSSION

Utilizing simple genetic engineering, we here report a new scFv-based therapeutic that is purified from

bacterial lysates using ELPs as a purification tag. We demonstrate the utility of ELPs as purification tag for bacterially expressed recombinant scFv. A similar approach illustrated by Topcic and co-workers<sup>36</sup> showed potent glycoprotein (GP) IIb/IIIa blocking *in vitro* and *in vivo* using a scFv ELP fusion. They also detail steric hindrance due to temperature-dependent  $\beta$ -turn maturation of the ELP.<sup>36</sup> This manuscript demonstrates that the scFv core of the nanoparticle remains accessible through the ELP corona and could be responsible for its activity.

Unique to this report, we observed that the fusion of ELPs and scFv produce highly potent nanoparticles. The formation of spherical or cylindrical particles by scFv-A192 could be due to recombinant scFv multimerization, which have been observed as dimers, trimers, and even hexamers.<sup>37,38</sup> To control this process of multimerization, the nanoparticle size was successfully reduced by guanidine refolding. This led to the formation of worm-like structures that efficiently target CD20 expressed on the surface of B-cell lymphomas. The formation of nanoworms was confirmed using cryoTEM, which showed particles of  $56.2 \pm 15.9$  nm in length. The nanoworms may assemble with a scFv core; however, these particles have a lower absolute molecular weight and relatively constant radius of gyration. Because of a lower mass distributed in the same volume after refolding, we hypothesize that the scFv core remains accessible, either at the end of the worms or through a loosely packed corona composed of the ELP protein polymer, which allows for potent CD20 recognition. The native scFv-A192 particles, which appear to be predominantly spherical, show partial signs of efficacy (Figure 7). This suggests that the scFv core remains biologically accessible even on round nanoparticles stabilized by a loosely packed ELP corona.

For the nanoworms, *in vitro* activity was first confirmed by measuring cell viability that showed selective killing of CD20+ cells albeit at a relatively high IC<sub>50</sub> (32 to 41  $\mu$ M). Compared to the poor reduction of

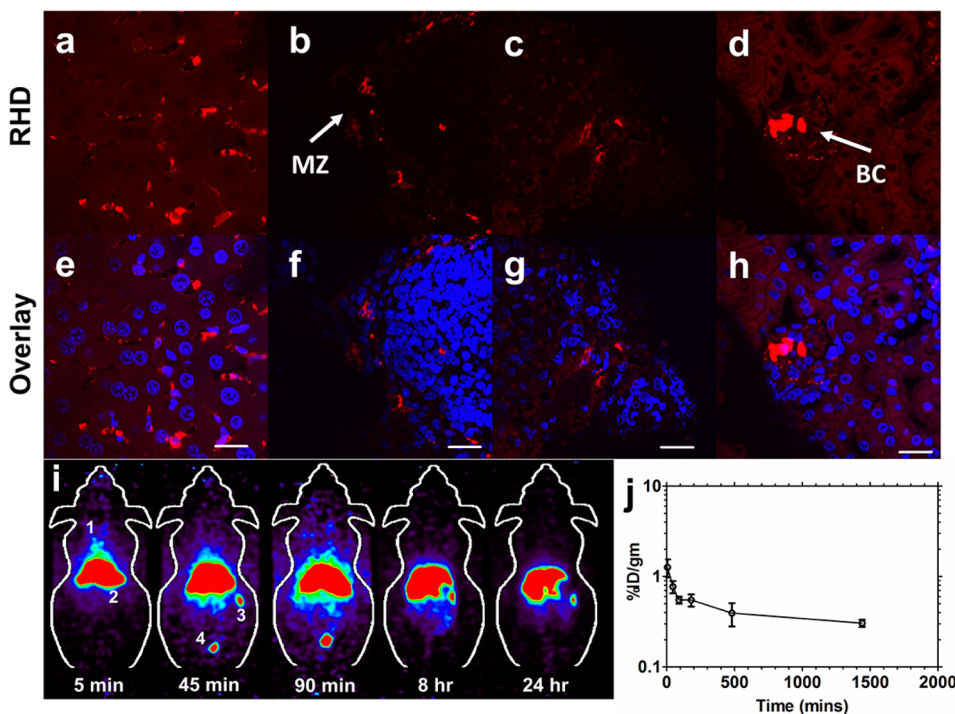


**Figure 8.** Nanoworms show high liver and splenic accumulation. (a–h) Nanoworm microbiodistribution (2.5 mg/dose,  $n = 3$ ) using laser confocal microscopy shows accumulation of rhodamine-labeled nanoworms in liver (a,e), spleen (b,f), tumor (c,g), and kidney (d,h). There was minimal accumulation of these particles in the lungs and heart. Interestingly, particle accumulation can be seen in the spleen marginal zone (MZ) and the bowman capsule (BC). The scale bar represents 20  $\mu\text{m}$ . (i) Nanoworms were complexed with  $^{64}\text{Cu}$  via a heterobifunctional sarcophagine chelator, AmBaSar. 100  $\mu\text{Ci}$  of active protein ( $\sim 0.2 \text{ mg}/\text{dose}$ ) were injected into Raji xenografted athymic nude mice ( $n = 3$ ). Nanoworms show high liver and spleen accumulation. (j) The heart activity half-life was obtained by selecting a three-dimensional region of interest with the same volume in all the reconstructed images. The half-life for nanoworm activity in the heart was calculated to be  $109.5 \pm 31.4 \text{ min}$ .

viability by Rituximab, however, the  $\text{IC}_{50}$  may be acceptable. The reduction in cell viability was confirmed to be due to the induction of apoptosis using independent techniques targeting different stages of apoptosis. Nanoworms greatly induced apoptosis ( $\sim 60\%$ ) in both cell lines and outperformed an equal Fv dose Rituximab treatment. Also, secondary GAH cross-linked Rituximab showed the same efficacy of induction as the nanoworm. Consistent with receptor-dependent apoptotic signaling, the nanoworm substantially activated caspase cascades in both cell lines. An unexpected observation was that Rituximab showed potent reduction in SU-DHL-7 viability using formazan-based assays despite minimal cell staining in both apoptosis assays. This contradiction may have arisen due to higher cell numbers used for the apoptosis staining experiments.

The *in vitro* activity of the nanoworms was successfully translated *in vivo* using a Raji cell xenograft. The treatment showed a significant delay in tumor growth when compared to Rituximab dosed at the equivalent mass of Fv variable fragments. The treatment dose for the nanoworm construct was chosen based on its activity *in vitro*. Tumor accumulation of the nanoworms was confirmed by injecting mice with a rhodamine-labeled reagent. The nanoworms showed visible liver, tumor, and spleen accumulation (Figure 8a–h).

The liver and spleen uptake is most likely attributed to the host reticuloendothelial system.<sup>39,40</sup> Kupffer cells in the liver are responsible for nanoparticle clearance<sup>41</sup> and hence may take up the nanoworms in circulation. In the spleen, the major nanoworm signal was present in the marginal zone lining the white pulp region (Figure 8b,f). The marginal zone is mainly populated by phagocytic macrophages and lymphocytes,<sup>42,43</sup> which play a significant role in filtering and clearing nanoparticles from the body.<sup>44,45</sup> Hence the liver and spleen signal could be due to phagocytosis and clearance by effector cells. This finding is consistent with the uptake of nanoparticles with similar size.<sup>46</sup> Interestingly, kidney sections also show entrapment of nanoparticles in the glomerulus, which is consistent with their high molecular weight (glomerulus filtration cut off  $\sim 60 \text{ kDa}$ ).<sup>47</sup> The splenic and hepatic accumulation of the nanoworm was confirmed using micropositron emission tomography (Figure 8i,j).

## CONCLUSION

This manuscript reports that fusions between protein polymers and a single-chain antibody can form high aspect ratio nanoparticles. Surprisingly, these nanoworms are highly potent effectors of the target of their scFv domain. These first generation nanoworms

(i) outperform a clinically successful monoclonal antibody (Rituximab) as a single agent, (ii) are likely biodegradable due to their peptidic nature, (iii) can be precisely tuned using genetic engineering, (iv) may be cheaper

to produce than mammalian expression of monoclonal antibodies, and (v) represent a simple platform to develop nanoparticles that bind targets of other therapeutic antibodies.

## MATERIALS AND METHODS

**Materials.** The DNA sequence encoding for anti-CD20 scFv (Table 1) was purchased from Integrated DNA Technologies (Coralville, IA). Cloning vector (Pet25b(+)), Top10, and Origami B(DE3) were purchased from Novagen (Darmstadt, Germany). Terrific broth dry powder was purchased from Mo-bio Laboratories (Carlsbad, CA). All restriction enzymes were purchased from New England Biolabs (Ipswich, MA). SYBR safe DNA stain, low and high melting point agarose, annexin V/propidium iodide apoptosis kit, and TUNEL staining kit were purchased from Invitrogen (Grand Island, NY). DNA mini prep and DNA purification kits were purchased from Qiagen (Germantown, MD). Bacteriological grade Agar and sodium chloride were purchased from Sigma Aldrich (St. Louis, MO). Nonradioactive cell viability MTS assay kit and CaspACE FITC-VAD-FMK *in situ* marker were purchased from Promega (Madison, WI). Precast 4–20% SDS PAGE gels were purchased from Lonza (Basel, Switzerland). Raji, CEM, SU-DHL-7, Rituximab, and chimeric Lym1 (chLym-1) antibodies were provided by Dr. Epstein (USC, Los Angeles, CA). Polyclonal goat antihuman Fc antibody (GAH) was purchased from Thermo Scientific (Rockford, IL). Cell culture media, Roswell Park Memorial Institute medium (RPMI 1640), was purchased from Corning (Tewksbury, MA). All cells were cultured in RPMI 1640 supplemented with 10% fetal bovine serum at 37 °C in humidified 5% carbon dioxide.

**Expression and Purification of scFv-A192 Fusions.** The anti-CD20 scFv was fused to ELPs using restriction enzyme digestion followed by sticky end ligation. The expressed protein was purified from bacterial lysates using temperature cycling. Briefly, the gene sequence encoding for an anti-CD20 scFv sequence (756 bp) was purchased in an ampicillin resistant proprietary pIDTsmart vector (Integrated DNA Technologies, IA). The scFv sequence was ligated into a pet25b(+) expression vector encoding the A192 ELP (Table 1) using restriction enzyme digestion. Sequence confirmed plasmid encoding for the scFv-A192 (Table 1) was transformed into chemically competent Origami B (DE3) *Escherichia coli* using heat shock at 42 °C for 5 min. Bacteria were plated onto ampicillin agar (100 µg/L) and incubated at 37 °C for 15–18 h and transformed colonies selected. The selected colonies were grown in 5 mL TB culture media with 100 µg/L of ampicillin for 15–18 h at 37 °C. The cultures were pelleted at 4000 rpm for 15 min and lysed to check for protein expression using SDS-PAGE. A colony with high protein expression was selected and grown in a 50 mL starter culture with 100 µg/L of ampicillin at 37 °C. The bacterial culture was then pelleted and inoculated into 1 L terrific broth media with 100 µg/L of ampicillin. The cultures were grown for 24 h, and bacteria were suspended in filtered PBS (4 L of culture in 25 mL of PBS) for downstream cell lysis. The bacteria were lysed using ultrasonication to release expressed cytosolic fusion protein, and bacterial DNA was precipitated using polyethyleneimine (50% w/v) at 12 000 rpm for 15 min. The supernatant containing the fusion protein was filtered through a 0.2 µm filter before protein purification using temperature cycling.<sup>48</sup>

The clarified lysate was equilibrated to room temperature, and ELP phase separation was induced by 3 M NaCl (i.e., for 50 mL of supernatant, 8 mg of NaCl was added). The ELP coacervate was collected at 25 °C for 20 min at 4000 rpm. The supernatant was discarded, and the pellet was solubilized in cold PBS. The solubilized pellet contains the ELP fusion with insoluble bacterial proteins that were removed at 4 °C under 12 000 rpm for 15 min. These hot and cold centrifugation cycles were repeated twice, and 6 M Guanidine HCl was added to disrupt the nanoparticles. To facilitate gradual renaturation of the scFv, guanidine salt was slowly removed using a dialysis

cassette with a 20 kDa molecular weight cut off against cold PBS at 4 °C. Dialysis was carried out with a 100:1 sink condition with 4 changes of buffer. A cold centrifugation was performed on the dialyzed protein, and a final temperature cycling step was performed to ensure removal of guanidine. The final protein stock was filtered through a sterile 0.2 µm filter, and protein concentration was determined using the Beer–Lambert law:

$$\text{concentration } (M) = \frac{A_{280} - A_{350}}{\text{MEC} \times l}$$

where  $A_{280}$  and  $A_{350}$  are the absorbance at 280 and 350 nm, respectively, MEC is the estimated molar extinction coefficient at 280 nm (67 900 M<sup>-1</sup> C<sup>-1</sup>), and  $l$  is the path length (cm).

### Determination of Purity and Transition Temperature of scFv-A192 Nanoparticles.

Purity of the constructs was determined using SDS-PAGE. Briefly, 10–15 µg of protein was added to SDS page loading buffer and boiled at 95 °C for 5 min. The sample was electrophoresed on 4–20% precast SDS-PAGE gel. After the samples are run the gel was stained using 50 mL of Coomassie Brilliant Blue R-250 solution (Biorad). The gel was imaged on a Biorad Versadoc imager (Hercules, CA) using white light. The purity of samples was calculated using ImageJ. Briefly, pictures were imported into ImageJ and converted to 8-bit files. Individual lanes were selected, and an intensity profile was extracted. The peak areas were calculated, and the purity was determined using the following equation:

$$\% \text{ purity} = \frac{A_{\text{peak}}}{A_{\text{tot}}} \times 100$$

where  $A_{\text{peak}}$  is the area of peak, and  $A_{\text{tot}}$  is the area under all of the peaks.

The transition temperature was characterized to confirm that the nanoworms remain soluble under physiological temperatures. Transition temperature was determined using optical density measurements at 350 nm in PBS. Briefly, increasing concentrations of constructs were added to 300 µL Beckman Coulter Tm microcells (Brea, CA), and the temperature was ramped at a rate of 1 °C/min. The optical density was plotted as a function of temperature, and the maximum first derivative of this curve was defined as the transition temperature.

**Light Scattering Analysis of Nanoparticles.** Light scattering was used to determine stability and assembly properties of nanoparticles. To prevent detection of artifacts, all buffers were sterile filtered using 0.45 µm filter. Dynamic light scattering was used to determine the hydrodynamic radius, temperature stability, and the polydispersity of the fusion proteins in solution. Briefly, increasing concentrations of the nanoparticles were pipetted into a 384-well clear bottom plate and measured using a Wyatt Dynapro plate reader (Santa Barbara, CA) using a 830 nm laser and a 1 °C/min temperature ramp from 20 to 45 °C.

Multiangle light scattering was used to determine the  $R_g$ , absolute molecular weight, and coordination number of the nanoparticles. The fusions were analyzed using tandem size exclusion chromatography and multiangle light scattering. Briefly, 250 µg of constructs were injected onto a Shodex size exclusion column using sterile filtered PBS at 0.5 mL/min. The column eluents were analyzed on a Wyatt Helios system (Santa Barbara, CA), and the data fit to a Debye plot to determine the  $R_g$  and the absolute molecular weight. The coordination number for the nanoparticles was determined by dividing the absolute molecular weight by the calculated monomeric scFv-A192 molecular weight. The  $R_g/R_h$  ratio was used to interpret the morphology of the particles.

**Electron Microscopy of Nanoparticles.** CryoTEM was performed to determine morphology in the presence of aqueous buffer.

Briefly, cryoTEM specimens were prepared using an FEI Vitrobot (Hillsboro, OR). Protein solutions were kept in an ice bath (4 °C) before processing and then raised to 37 °C immediately prior to blotting. Six microliters of sample were pipetted onto a TEM grid coated with a lacey carbon film (LC325-Cu, Electron Microscopy Sciences). The specimen was then blotted under 95% humidity, immediately transferred into liquid ethane, and stored in liquid nitrogen environment. Micrographs were acquired using FEI Tecnai 12 TWIN TEM equipped with 16 bit 2Kx2K FEI eagle bottom mount camera (Hillsboro, OR). All cryoTEM images were acquired at an accelerating voltage of 100 kV. Images were analyzed using ImageJ (NIH, USA).

**Secondary Structure Determination Using Circular Dichroism.** Circular dichroism was performed to determine the secondary structure of the polypeptide nanoparticles. The constructs were run on a Jasco J-815 spectrometer (Easton, MD) using a quartz cuvette (path length ~1 mm). The ellipticity was monitored from 185 to 250 nm, and the spectra of buffer subtracted postrun. All the constructs were prepared in filtered distilled deionized water. Deconvolution was performed under the assumption that the observed molar ellipticity [ $\theta$ ] is a weighted linear sum of the ellipticity for known secondary structures. The data was fit using nonlinear regression on Microsoft Excel using the following relationship:

$$\theta = \sum \theta_{\text{std}} C_{\text{std}}$$

where  $\theta$  is the observed ellipticity,  $\theta_{\text{std}}$  is the ellipticity of standard, and  $C_{\text{std}}$  is the fraction of standard.

**In Vitro CD20 Recognition Using Confocal Laser Scanning Microscopy.** CD20 recognition was tested in CD20+ and CD20− cells. For CD20+ cells, Burkitt's (Raji) and diffuse large B-cell lymphoma (SU-DHL-7) cell lines were evaluated. A T-acute lymphoblastic leukemia, CEM cell line was used as a CD20− control. CD20 recognition was performed using rhodamine-labeled proteins imaged by confocal laser scanning microscopy. Briefly, 50 µg of rhodamine-labeled nanoworms or Rituximab was added to 1 mL of  $2 \times 10^5$  cells suspended in 1% bovine serum albumin in Dulbecco's PBS. The cells were incubated with 50 µg of labeled protein for 15 min at room temperature with occasional agitation. After incubation, cells were transferred to 3 mL tubes and centrifuged at 750 rpm for 5 min to remove unbound proteins. The cell pellets were washed twice with Dulbecco's PBS and suspended in 100 µL of 1% bovine serum albumin in Dulbecco's PBS. The cells were mounted onto glass slides and observed under a Zeiss LSM510 confocal microscope with a 543 nm green excitation laser. For Rituximab competition studies, the cells were incubated with 1 mg of unlabeled antibody for 15 min, washed, and incubated with rhodamine-labeled nanoworms as above. GAH cross-linked Rituximab was imaged after a 15 min incubation with 10 µg of GAH. After incubation, the cells were washed and imaged. Images were analyzed using ImageJ.

**Cell Viability Assays.** A formazan-based colorimetric assay was used to determine cell viability. Viability assays were performed on Raji, SU-DHL-7, and CEM cells. All assays were performed in 10% fetal bovine serum in RPMI 1640 supplemented with Penn-Strep antibiotics. Briefly,  $2 \times 10^4$  cells/well were pipetted in to 96-well plates, and serial dilutions of nanoworm and Rituximab were added in triplicates. RPMI 1640 with appropriate protein dilution was used as a blank control. The cells were incubated with the protein for 24 h under humidified 5% carbon dioxide, after which 30 µL of MTS/PMS was added to determine viability. The cells were incubated for 2 h and read at 490 nm using a Biorad benchmark plus plate reader (Hercules, CA). The percentage cell viability was calculated and plotted versus protein concentration using the following equation:

$$\% \text{cell viability} = \frac{(A_{\text{treated}} - A_{\text{cont}}) \times 100}{(A_{\text{untreated}} - A_0)}$$

where  $A_{\text{treated}}$  is the absorbance of treated cells at 490 nm,  $A_{\text{cont}}$  is the absorbance of control wells at 490 nm,  $A_{\text{untreated}}$  is the absorbance of untreated cell absorbance at 490 nm, and  $A_0$  is the absorbance at 490 nm with no cells.

**Detection of Apoptosis and Caspase Activation Using Flow Cytometry.** Induction of apoptosis was determined using early and late stage apoptotic markers. Annexin V/propidium iodide staining was used to detect early induction of apoptosis. An antibody against HLA-Dr10 tumor cells, chLym-1, was used as a positive control for direct induction of apoptosis. Briefly,  $2 \times 10^5$  cells/well in 10% fetal bovine serum in RPMI 1640 supplemented with Penn-Strep were added to a 12 well plate. The cells were incubated with equivalent scFv concentrations (1.5 mg/mL) of the nanoworm, ELP, Rituximab, Rituximab + secondary GAH and chLym-1 at 37 °C with humidified 5% carbon dioxide for 18 h. For annexin V+ and propidium iodide+ compensation controls, cells were treated with 50 µg of paclitaxel and analyzed before test samples. For secondary GAH-mediated cross-linking the cells were incubated with Rituximab for 30 min, washed, and incubated with 100 µg of secondary GAH in fresh cell culture media for 18 h. After incubation the cells were centrifuged, washed twice with PBS, and suspended in 100 µL of annexin V staining buffer. The cells were stained with annexin V and propidium iodide as per the manufacturer's instructions; i.e., 5 µL of AlexaFluor 488-annexin V stock and 1 µL of 5-fold diluted propidium iodide stock were added to the cell and incubated for 15 min. The volume of cells was made up to 500 µL with annexin V binding buffer and analyzed on an Attune acoustic focusing flow cytometer (Life Technologies, Grand Island, NY). The data were analyzed using Flowjo software (Ashland, OR).

Late stage apoptosis was detected using terminal deoxy-nucleotidyl transferase dUTP nick end labeling (TUNEL). The labeling was performed as per the manufacturer's protocol. Briefly,  $2 \times 10^6$  cells/well in 10% fetal bovine serum in RPMI 1640 supplemented with Penn-Strep were added to a 12 well plate. The cells were treated with equivalent scFv concentrations (2.5 mg/mL) of the nanoworm, Rituximab, and Rituximab + secondary GAH and incubated at 37 °C with humidified 5% carbon dioxide for 18 h. The Rituximab cross-linking by secondary goat antihuman Fc antibody was performed similar to annexin V/propidium iodide staining. TUNEL staining was performed as per manufacturer's protocol. Briefly, treated cells were washed with PBS and fixed in 1% formaldehyde for 15 min and dehydrated using 70% ethanol for 5 h on ice. The fixed cells were washed, transferred to a BrdUTP labeling buffer, and labeled with BrdU overnight at room temperature. After completion of reaction Alexa488 labeled anti-BrdUTP antibody was added and incubated for 2 h. Propidium iodide was added 30 min before sample analysis, and data were collected as .fcs files. Analysis was performed using Flowjo (Ashland, OR).

Activation of the caspase cascade (caspase 3, 8, and 9) was detected using a FITC labeled cell penetrating irreversible caspase inhibitor, Z-VAD-FMK (carbobenzoxy-valyl-alanyl-aspartyl-fluoromethylketone).<sup>49</sup> VAD-FMK binds different caspases with varying affinities.<sup>49</sup> Briefly,  $2 \times 10^5$  cells/well in 10% fetal bovine serum in RPMI 1640 supplemented with Penn-Strep were added to 12 well plate, and nanoworm (Fv dose-1.5 mg/mL) added to appropriate wells. The cells were incubated at 37 °C with humidified 5% carbon dioxide for 18 h. After incubation 2 µL of 20 mM FITC-VAD-FMK were added to 1 mL of culture. The cells were incubated for 1 h at 37 °C with humidified 5% carbon dioxide. The labeled cells were washed with PBS, fixed in 4% formaldehyde, and analyzed using flow cytometry. Recorded data was analyzed using Flowjo (Ashland, OR).

**In Vivo Tumor Regression and Biodistribution Studies.** Human Burkitt's lymphoma xenografts (Raji) were used to determine *in vivo* efficacy of scFv constructs. All procedures performed were in accordance to the university approved IACUC protocol. Briefly, Athymic nude mice were irradiated using an X-ray irradiator (400 rads) to lower their NK cell population and allowed to recover for 24 h. After recovery, a 200 µL inoculum of  $5 \times 10^6$  Raji cells and  $1 \times 10^5$  human fetal fibroblasts (used to support early tumor growth) were implanted subcutaneously on the right flank of the mouse. The mice were divided into 3 treatment groups ( $n = 5$ ): PBS, Rituximab (1.7 mg/dose), and the nanoworm (scFv-A192, 2.5 mg/dose). Rituximab and the nanoworms were dosed at an equivalent variable fragment dose of 600 µg. Animal dosing was started once all tumors

reached 150 mm<sup>3</sup>, and the total number of doses was limited to 8 per mouse. The first two doses were administered on consecutive days, and the following six doses given every other day. Animal weight and tumor volumes were monitored every other day, and measurements were blinded to the treatment group. Animals were euthanized at the humane end point of a tumor volume (1000 mm<sup>3</sup>) or because of the occurrence of any adverse reactions to treatment. Organs from sacrificed animals were harvested and fixed in zinc formalin for 18 h and dehydrated in 70% alcohol for 24 h before paraffin embedding. After dehydration, the dry weights of the liver, spleen, and tumor were recorded. After paraffin embedding, fine 5 µm slices of the organs were stained with hematoxylin and eosin and studied for histological changes. The tumor volume for this study was calculated using the following formula:

$$\text{tumor volume} = \frac{\pi}{6}(w^2 \times l)$$

where *w* and *l* are the width and length of the tumor, respectively.

*In vivo* biodistribution studies were performed using rhodamine-labeled nanoworms in Raji xenografted mice (*n* = 3). A therapeutic dose of 2.5 mg was administered to the animals, and the animals were sacrificed after 8 h. The organs of the animals were harvested, fixed in zinc formalin for 18 h, and dehydrated in 70% alcohol for 24 h prior to paraffin embedding. Paraffin was removed, and the sections were permeabilized with 10% sodium dodecyl sulfate (SDS). The nuclei were stained by incubation in a 1:1000 dilution of 4,6-diamidino-2-phenylindole (DAPI) for 1 h. After incubation, the sections were washed with 1% bovine serum albumin in PBS and treated with antifade reagent. The slides were dried overnight and imaged under a Zeiss LSM510 confocal laser scanning microscope. 543 and 790 nm excitation lasers were used to image rhodamine and DAPI, respectively. All images were processed on ImageJ.

Further biodistribution studies were performed using radiolabeled fusion proteins. The proteins were complexed with <sup>64</sup>Cu heterobifunctional sarcophagine chelator, AmBaSar and 100–110 µCi of active protein (~0.2 mg/dose) injected into Raji xenografted nude mice (*n* = 3).<sup>50</sup> The animals were analyzed at set time points using a microPET Sophie Genisys4 (Culver City, CA). The data was recorded as DICOM files, and images were reconstructed on AMIDE 1.0.4. The heart activity half-life was estimated by selecting a 3D region of interest with the same volume in all the reconstructed images.

**Conflict of Interest:** The authors declare no competing financial interest.

**Acknowledgment.** This work was made possible by the University of Southern California, the National Institute of Health R21EB012281 to J.A.M., and P30 CA014089 to the Norris Comprehensive Cancer Center, the USC Molecular Imaging Center, the USC Nanobiophysics Core Facility, the Translational Research Laboratory at the School of Pharmacy, the American Cancer Society IRG-58-007-48, the Stop Cancer Foundation, the USC Ming Hsieh Institute, the USC Whittier Foundation, and the USC Wright Foundation.

**Supporting Information Available:** *In vitro* and *in vivo* results of supporting experiments. This material is available free of charge via the Internet at <http://pubs.acs.org.org>.

## REFERENCES AND NOTES

- Holliger, P.; Hudson, P. J. Engineered Antibody Fragments and the Rise of Single Domains. *Nat. Biotechnol.* **2005**, *23*, 1126–1136.
- Melmed, G. Y.; Targan, S. R.; Yasothan, U.; Hanicq, D.; Kirkpatrick, P. Certolizumab Pegol. *Nat. Rev. Drug Discovery* **2008**, *7*, 641–642.
- Nelson, A. L. Antibody Fragments: Hope and Hype. *mAbs* **2010**, *2*, 77–83.
- Weisser, N. E.; Hall, J. C. Applications of Single-Chain Variable Fragment Antibodies in Therapeutics and Diagnostics. *Biotechnol. Adv.* **2009**, *27*, 502–520.
- Qian, X.; Peng, X. H.; Ansari, D. O.; Yin-Goen, Q.; Chen, G. Z.; Shin, D. M.; Yang, L.; Young, A. N.; Wang, M. D.; Nie, S. *In Vivo* Tumor Targeting and Spectroscopic Detection with Surface-Enhanced Raman Nanoparticle Tags. *Nat. Biotechnol.* **2008**, *26*, 83–90.
- Rudnick, S. I.; Adams, G. P. Affinity and Avidity in Antibody-Based Tumor Targeting. *Cancer Biother. Radiopharm.* **2009**, *24*, 155–161.
- King, D. J.; Turner, A.; Farnsworth, A. P. H.; Adair, J. R.; Owens, R. J.; Pedley, R. B.; Baldock, D.; Proudfoot, K. A.; Lawson, A. D. G.; Beeley, N. R. A.; et al. Improved Tumor Targeting with Chemically Cross-Linked Recombinant Antibody Fragments. *Cancer Res.* **1994**, *54*, 6176–6185.
- Yokota, T.; Milenic, D. E.; Whitlow, M.; Schlom, J. Rapid Tumor Penetration of a Single-Chain Fv and Comparison with Other Immunoglobulin Forms. *Cancer Res.* **1992**, *52*, 3402–3408.
- Cumber, A. J.; Ward, E. S.; Winter, G.; Parnell, G. D.; Wawrzynszak, E. J. Comparative Stabilities *In Vitro* and *In Vivo* of a Recombinant Mouse Antibody Fvcys Fragment and a Bisfvcs Conjugate. *J. Immunol.* **1992**, *149*, 120–126.
- Schneider, D. W.; Heitner, T.; Alicke, B.; Light, D. R.; McLean, K.; Satozawa, N.; Parry, G.; Yoo, J.; Lewis, J. S.; Parry, R. *In Vivo* Biodistribution, Pet Imaging, and Tumor Accumulation of 86y- and 111In-Antimedin/Rg-1, Engineered Antibody Fragments in Lncap Tumor-Bearing Nude Mice. *J. Nucl. Med.* **2009**, *50*, 435–443.
- Müller, D.; Karle, A.; Meißenburger, B.; Höfig, I.; Stork, R.; Kontermann, R. E. Improved Pharmacokinetics of Recombinant Bispecific Antibody Molecules by Fusion to Human Serum Albumin. *J. Biol. Chem.* **2007**, *282*, 12650–12660.
- Yang, K.; Basu, A.; Wang, M.; Chintala, R.; Hsieh, M. C.; Liu, S.; Hua, J.; Zhang, Z.; Zhou, J.; Li, M.; et al. Tailoring Structure–Function and Pharmacokinetic Properties of Single-Chain Fv Proteins by Site-Specific Pegylation. *Protein Eng., Des. Sel.* **2003**, *16*, 761–770.
- Howlader, N.; Noone, A. M.; Krapcho, M.; Garshell, J.; Neyman, N.; Altekruse, S. F.; Kosary, C. L.; Yu, M.; Ruhl, J.; Tatalovich, Z.; Cho, H.; Mariotto, A.; Lewis, D. R.; Chen, H. S.; Feuer, E. J.; Cronin, K. A. *SEER Cancer Statistics Review, 1975–2010*; National Cancer Institute: Bethesda, MD, 2013; [http://seer.cancer.gov/csr/1975\\_2010/](http://seer.cancer.gov/csr/1975_2010/).
- Coiffier, B.; Lepage, E.; Brière, J.; Herbrecht, R.; Tilly, H.; Bouabdallah, R.; Morel, P.; Van Den Neste, E.; Salles, G.; Gaulard, P.; et al. Chop Chemotherapy Plus Rituximab Compared with Chop Alone in Elderly Patients with Diffuse Large-B-Cell Lymphoma. *N. Engl. J. Med.* **2002**, *346*, 235–242.
- Fitoussi, O.; Belhadj, K.; Mounier, N.; Parrens, M.; Tilly, H.; Salles, G.; Feugier, P.; Ferme, C.; Ysebaert, L.; Gabarre, J.; et al. Survival Impact of Rituximab Combined with Acvbp and Upfront Consolidation Autotransplantation in High-Risk Diffuse Large B-Cell Lymphoma for Gela. *Haematologica* **2011**, *96*, 1136–1143.
- Webber, D. Lymphoma Mabs Rivalry Continues. *Nat. Biotechnol.* **1998**, *16*, 1000–1001.
- Sousou, T.; Friedberg, J. Rituximab in Indolent Lymphomas. *Semin. Hematol.* **2010**, *47*, 133–142.
- Weiner, G. J. Rituximab: Mechanism of Action. *Semin. Hematol.* **2010**, *47*, 115–123.
- Zhang, N.; Khawli, L. A.; Hu, P.; Epstein, A. L. Generation of Rituximab Polymer May Cause Hyper-Cross-Linking-Induced Apoptosis in Non-Hodgkin's Lymphomas. *Clin. Cancer Res.* **2005**, *11*, 5971–5980.
- Unruh, T. L.; Li, H.; Mutch, C. M.; Sharlat, N.; Grigoriou, L.; Sanyal, R.; Brown, C. B.; Deans, J. P. Cholesterol Depletion Inhibits Src Family Kinase-Dependent Calcium Mobilization and Apoptosis Induced by Rituximab Crosslinking. *Immunology* **2005**, *116*, 223–232.
- Roda, J. M.; Byrd, J. C. FcγRIIIa Role in Rituximab Efficacy. *Blood* **2007**, *110*, 2220.
- Semac, I.; Palomba, C.; Kulangara, K.; Klages, N.; van Echten-Deckert, G.; Borisch, B.; Hoessli, D. C. Anti-CD20 Therapeutic Antibody Rituximab Modifies the Functional Organization of Rafts/Microdomains of B Lymphoma Cells. *Cancer Res.* **2003**, *63*, 534–540.

23. Deans, J. P.; Li, H.; Polyak, M. J. CD20-Mediated Apoptosis: Signalling through Lipid Rafts. *Immunology* **2002**, *107*, 176–182.
24. Jazirehi, A. R.; Bonavida, B. Cellular and Molecular Signal Transduction Pathways Modulated by Rituximab (Rituxan, Anti-CD20 Mab) in Non-Hodgkin's Lymphoma: Implications in Chemosensitization and Therapeutic Intervention. *Oncogene* **2005**, *24*, 2121–2143.
25. Rossi, E. A.; Goldenberg, D. M.; Cardillo, T. M.; Stein, R.; Wang, Y.; Chang, C.-H. Novel Designs of Multivalent Anti-CD20 Humanized Antibodies as Improved Lymphoma Therapeutics. *Cancer Res.* **2008**, *68*, 8384–8392.
26. Johnson, R. N.; Kopečková, P.; Kopeček, J. i. Synthesis and Evaluation of Multivalent Branched Hpma Copolymer–Fab' Conjugates Targeted to the B-Cell Antigen CD20. *Bioconjugate Chem.* **2008**, *20*, 129–137.
27. Urry, D. W. Physical Chemistry of Biological Free Energy Transduction as Demonstrated by Elastic Protein-Based Polymers. *J. Phys. Chem. B* **1997**, *101*, 11007–11028.
28. Schmidt, M.; Stockmayer, W. H. Quasi-Elastic Light Scattering by Semiflexible Chains. *Macromolecules* **1984**, *17*, 509–514.
29. Moffitt, M.; Yu, Y.; Nguyen, D.; Graziano, V.; Schneider, D. K.; Eisenberg, A. Coronal Structure of Star-Like Block Ionomer Micelles: An Investigation by Small-Angle Neutron Scattering. *Macromolecules* **1998**, *31*, 2190–2197.
30. Zhang, N.; Khawli, L. A.; Hu, P.; Epstein, A. L. Lym-1-Induced Apoptosis of Non-Hodgkin's Lymphomas Produces Regression of Transplanted Tumors. *Cancer Biother. Radiopharm.* **2007**, *22*, 342–356.
31. Tobin, E.; Denardo, G.; Zhang, N.; Epstein, A. L.; Liu, C.; Denardo, S. Combination Immunotherapy with Anti-CD20 and Anti-HLA-Dr Monoclonal Antibodies Induces Synergistic Anti-Lymphoma Effects in Human Lymphoma Cell Lines. *Leuk. Lymphoma* **2007**, *48*, 944–956.
32. Rimsza, L. M.; Roberts, R. A.; Miller, T. P.; Unger, J. M.; LeBlanc, M.; Braziel, R. M.; Weisenberger, D. D.; Chan, W. C.; Muller-Hermelink, H. K.; Jaffe, E. S.; et al. Loss of MHC Class II Gene and Protein Expression in Diffuse Large B-Cell Lymphoma Is Related to Decreased Tumor Immunosurveillance and Poor Patient Survival Regardless of Other Prognostic Factors: A Follow-up Study from the Leukemia and Lymphoma Molecular Profiling Project. *Blood* **2004**, *103*, 4251–4258.
33. Dahle, J.; Borrebaek, J.; Jonasdottir, T. J.; Hjelmerud, A. K.; Melhus, K. B.; Bruland, O. S.; Press, O. W.; Larsen, R. H. Targeted Cancer Therapy with a Novel Low-Dose Rate Alpha-Emitting Radioimmunoconjugate. *Blood* **2007**, *110*, 2049–2056.
34. Clynes, R. A.; Towers, T. L.; Presta, L. G.; Ravetch, J. V. Inhibitory Fc Receptors Modulate *In Vivo* Cytotoxicity against Tumor Targets. *Nat. Med.* **2000**, *6*, 443–446.
35. Dayde, D.; Ternant, D.; Ohresser, M.; Lerondel, S.; Pesnel, S.; Watier, H.; Le Pape, A.; Bardos, P.; Paintaud, G.; Cartron, G. Tumor Burden Influences Exposure and Response to Rituximab: Pharmacokinetic-Pharmacodynamic Modeling Using a Syngeneic Bioluminescent Murine Model Expressing Human CD20. *Blood* **2009**, *113*, 3765–3772.
36. Topcic, D.; Kim, W.; Holien, J. K.; Jia, F.; Armstrong, P. C.; Hohmann, J. D.; Straub, A.; Krippner, G.; Haller, C. A.; Domeij, H.; et al. An Activation-Specific Platelet Inhibitor That Can Be Turned On/Off by Medically Used Hypothermia. *Arterioscler., Thromb., Vasc. Biol.* **2011**, *31*, 2015–2023.
37. Dolezal, O.; Pearce, L. A.; Lawrence, L. J.; McCoy, A. J.; Hudson, P. J.; Kortt, A. A. Scfv Multimers of the Anti-Neuraminidase Antibody Nc10: Shortening of the Linker in Single-Chain Fv Fragment Assembled in VI to Vh Orientation Drives the Formation of Dimers, Trimmers, Tetramers and Higher Molecular Mass Multimers. *Protein Eng., Des. Sel.* **2000**, *13*, 565–574.
38. Kortt, A. A.; Dolezal, O.; Power, B. E.; Hudson, P. J. Dimeric and Trimeric Antibodies: High Avidity Scfvs for Cancer Targeting. *Biomol. Eng.* **2001**, *18*, 95–108.
39. Brigger, I.; Dubernet, C.; Couvreur, P. Nanoparticles in Cancer Therapy and Diagnosis. *Adv. Drug Delivery Rev.* **2002**, *54*, 631–651.
40. Buzea, C.; Pacheco, I. I.; Robbie, K. Nanomaterials and Nanoparticles: Sources and Toxicity. *Biointerphases* **2007**, *2*, MR17–MR71.
41. Dobrovolskaia, M. A.; Germolec, D. R.; Weaver, J. L. Evaluation of Nanoparticle Immunotoxicity. *Nat. Nanotechnol.* **2009**, *4*, 411–414.
42. Martin, F.; Kearney, J. F. Marginal-Zone B Cells. *Nat. Rev. Immunol.* **2002**, *2*, 323–335.
43. Kraal, G. Cells in the Marginal Zone of the Spleen. *Int. Rev. Cytol.* **1992**, *132*, 31–74.
44. Aichele, P.; Zinke, J.; Grode, L.; Schwendener, R. A.; Kaufmann, S. H. E.; Seiler, P. Macrophages of the Splenic Marginal Zone Are Essential for Trapping of Blood-Borne Particulate Antigen but Dispensable for Induction of Specific T Cell Responses. *J. Immunol.* **2003**, *171*, 1148–1155.
45. Demoy, M.; Andreux, J. P.; Weingarten, C.; Gouritin, B.; Guilloux, V.; Couvreur, P. Spleen Capture of Nanoparticles: Influence of Animal Species and Surface Characteristics. *Pharm. Res.* **1999**, *16*, 37–41.
46. Moghimi, S. M.; Hunter, A. C.; Andrensen, T. L. Factors Controlling Nanoparticle Pharmacokinetics: An Integrated Analysis and Perspective. *Annu. Rev. Pharmacol. Toxicol.* **2012**, *52*, 481–503.
47. Meibohm, B.; Zhou, H. Characterizing the Impact of Renal Impairment on the Clinical Pharmacology of Biologics. *J. Clin. Pharmacol.* **2012**, *52*, 545–625.
48. Hassouneh, W.; Christensen, T.; Chilkoti, A. Elastin-Like Polypeptides as a Purification Tag for Recombinant Proteins. *Curr. Protoc. Protein Sci.* **2010**, *61*, 6.11.1–6.11.16.
49. Slee, E. A.; Zhu, H.; Chow, S. C.; MacFarlane, M.; Nicholson, D. W.; Cohen, G. M. Benzylloxycarbonyl-Val-Ala-Asp (Ome) Fluoromethylketone (Z-Vad.Fmk) Inhibits Apoptosis by Blocking the Processing of Cpp32. *Biochem. J.* **1996**, *315* (Pt 1), 21–24.
50. Janib, S. M.; Liu, S.; Park, R.; Pastuszka, M. K.; Shi, P.; Moses, A. S.; Orosco, M. M.; Lin, Y. A.; Cui, H.; Conti, P. S.; et al. Kinetic Quantification of Protein Polymer Nanoparticles Using Non-Invasive Imaging. *Integr. Biol.* **2013**, *5*, 183–194.